FISHVIER

Contents lists available at ScienceDirect

Powder Technology

journal homepage: www.elsevier.com/locate/powtec



Three-dimensional particle shape characterizations from half particle geometries



Junxing Zheng a,*, Quan Sun a, Hang Zheng b, Deheng Wei c, Zhaochao Li d, Lin Gao e

- ^a Department of Civil, Construction and Environmental Engineering, Iowa State University, Ames, IA 50011, USA
- ^b Department of Mechanical Engineering, Guizhou university, Guiyang, Guizhou, China
- ^c School of Civil Engineering, The University of Sydney, Sydney, Australia
- ^d Morehead State University, Morehead, KY 40351, USA
- ^e Ivy College of Business, Iowa State University, Ames, IA 50011, USA

ARTICLE INFO

Article history: Received 24 January 2020 Received in revised form 15 March 2020 Accepted 22 March 2020 Available online 23 March 2020

Keywords: Particle shape characterization Granular soil Computational geometry Structured light X-ray computed tomography

ABSTRACT

Many three-dimensional (3D) imaging techniques, such as 3D laser scanner, stereophotography, and structured light techniques, can only capture upper half particle geometries in the camera view, and lower half particle geometries are occluded from the camera. This research aims to evaluate the accuracy of using half particle geometries to compute 3D particle shape descriptors. Computational geometry techniques are developed to compute eight commonly used particle shape descriptors automatically. Five coarse sand specimens are scanned by X-ray computed tomography and structured light to generate full 3D and half particle geometries, respectively. The convexity, diameter sphericity, and surface area sphericity computed from half particles overestimate these values computed from full 3D particles, which are corrected by statistical equations. The circularity, volume sphericity, intercept sphericity, sphere ratio sphericity, and roundness computed from half particles agreed excellently with these values computed from 3D particles.

 $\ensuremath{\mathbb{C}}$ 2020 Elsevier B.V. All rights reserved.

1. Introduction

Particle shape is a fundamental property of granular soils governing the capability of particles for forming interparticle locking. Angular and elongated particles have many sharp protrusions (or corners), which interlock with each other to form a larger coordination number and a stronger load-bearing skeleton. Therefore, experimental and numerical studies have shown that angular and elongated soils exhibit larger values of index void ratios, angle of internal friction, dilatancy, constant volume friction angle, and small-strain modulus than rounded and spherical soils [1–5].

Traditionally, two-dimensional (2D) maximum particle projections were used to characterize particle shapes through either manual measurements or visual comparisons to reference charts [6–8]. The manual method was tedious, and the visual comparison method was subjective. Both methods were difficult to implement on a large number of particles [9]. Advances in optical image gathering have led to the rapid digitization of soil particle projections. Therefore, image processing algorithms have been developed to automate the computations of 2D shape descriptors in the last two decades [10–12]. The image-based particle shape characterizations enabled researchers to rapidly and

E-mail addresses: junxing@iastate.edu (J. Zheng), quansun@iastate.edu (Q. Sun), dwei3017@uni.sydney.edu.au (D. Wei), mli@moreheadstate.edu (Z. Li).

effectively quantify the shapes and sizes of a large number of particles. However, the 2D particle projections were limited to characterize three-dimensional (3D) particle shapes. Therefore, researchers were developing 3D imaging techniques for better analyzing particle shapes.

The X-ray Computed Tomography (X-ray CT) is an ideal technique to capture the full 3D particle surface geometries, and many geotechnical researchers have used this technique to analyze particle shapes [13–20]. However, the shortcomings of X-ray CT are apparent. First, the initial cost of an X-ray CT device is high, and an experienced technician is required to operate and maintain it. Second, because of constraints of resolution and field of view, the X-ray CT can only scan a small specimen. The scanned specimen sizes reported in the literature were typically 12 mm in diameter and 24 mm in height. Third, processing X-ray CT images is computationally demanding and time-consuming, requiring high-performance computing resources.

Researchers have developed other techniques that are low-cost and easy-to-implement to scan 3D particle surface geometries. Kim et al. [21] developed a laser scanning system to obtain the 3D particle geometries. Zheng and Hryciw [22,23] introduced a low-cost and simple stereophotography system to capture 3D particle geometries. Sun et al. [24] proposed a structured light system to capture 3D particle geometries. The laser scanning, stereophotography, and structured light systems can rapidly capture 3D geometries of many particles from medium sand to gravel sizes. Compared with X-ray CT, these systems are simple and low-cost and can be easily constructed in common soil

^{*} Corresponding author.

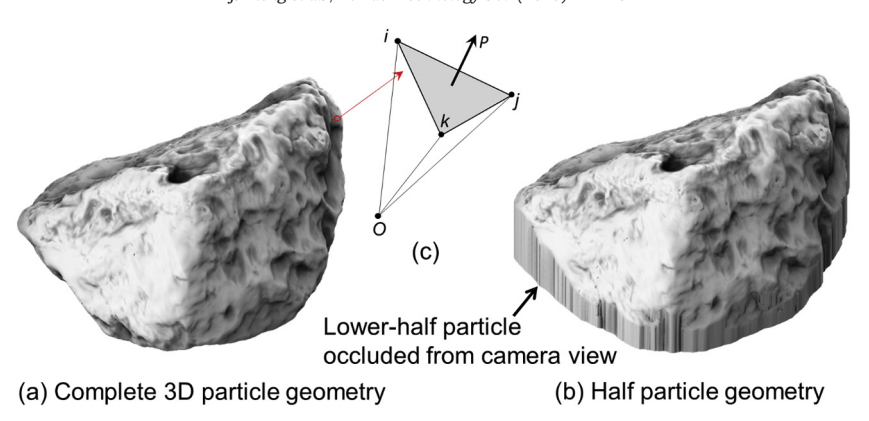


Fig. 1. Comparisons between complete and half particle geometries.

testing laboratories. However, these systems have limitations: they can only capture the upper-half particle surfaces exposed to the camera view or half particle geometries. For example, Fig. 1(a) shows a complete 3D particle geometry scanned by X-ray CT. The same particle was captured by the structured light system developed by Sun et al. [24] as shown in Fig. 1(b). The lower-half particle geometry is occluded from the camera view.

Based on Lee and Chang [25], this paper defines the upper-half particle geometries captured by the laser scanner, stereophotography, and structured light as "2.5D" particle geometries in contrast with the full 3D particle geometries obtained by X-ray CT. Zheng and Hryciw [23] and Sun et al. [24] have extensively compared the particle size distributions determined from 2.5D particle geometries with sieve analysis results. They found excellent agreements, demonstrating that 2.5D particles provided accurate particle size characterizations. This was somewhat expected. The 2.5D image geometries yielded accurate results of three principal dimensions of particles (i.e., length, width, and thickness), and the particle width and thickness determined the square sieve openings through which the particle can pass [26].

However, it is unknown whether the 2.5D particles can provide accurate particle shape characterizations. Particle shape is commonly quantified by sphere and roundness as shown in Table 1. Sphericity quantifies how closely the overall shape of the particle conforms to a perfect sphere. At the smaller scale level, roundness quantifies the angularity of particles. Many sphericity definitions have been proposed as shown in Table 1. However, the basic idea of these definitions is

essentially the same. They compare the surface area of a particle with the surface area of a sphere having the same volume as the particle, or compare the volume of a particle with the volume of a sphere having the same surface area as the particle, or compare the length, width, and thickness of a particle.

In this paper, we evaluate the accuracy of using 2.5D geometries for determining these eight shape descriptors in Table 1. This paper develops a series of computational geometry algorithms to compute these shape descriptors from 3D or 2.5D particle geometries. Then, five coarse sand specimens with a range of particle shapes are captured by both X-ray CT and structured light to obtain their 3D and 2.5D geometries. The particle shape descriptors from 3D and 2.5D geometries are computed using the developed computational geometry algorithm, and the results are compared.

2. Methods

2.1. Computational geometry algorithm for determining sphericity descriptors

Computations of 3D sphericity descriptors in Table 1 require parameters including principal dimensions, volume, surface area, minimum circumscribed sphere, maximum inscribed sphere, and 3D convex hull.

In computer graphics, the 3D geometries are represented by triangular face tessellations. For example, the 3D soil particle in Fig. 1 (a) consists of 44,762 triangles and 22,383 vertices. The 2.5D particle

Table 1Commonly used shape descriptors and their definitions.

Definitions (reference)	Formula	Note
Sphericity		
Convexity (solidity) [30]	$C_x = \frac{V}{V_c}$	The ratio of the volume of the particle (V) to the volume of the minimum convex hull circumscribing the particle (V_c) .
Circularity [31]	$C_x = \frac{V}{V_c}$ $C = \frac{6V}{\sqrt{\frac{A_s^3}{\pi}}}$	The ratio of the volume of the particle (V) to the volume of the sphere having the same surface area (A_s) as the particle.
Intercept sphericity [7]	$S_{I} = \sqrt[3]{\frac{d_{2}d_{3}}{d_{1}^{2}}}$ $S_{V} = \frac{V}{V_{cir}}$ $S_{D} = \frac{D_{e}}{D_{c}}$ $S_{C} = \frac{D_{i}}{D_{c}}$ $S_{A} = \frac{A_{e}}{A_{s}}$	The cubic root of ratio of the product of the width of the particle (d_2) and the thickness of the particle (d_3) to the square of the length of the particle (d_1) .
Volume sphericity [32]	$S_V = \frac{V}{V_{cir}}$	The ratio of the volume of the particle (V) to the volume of the smallest circumscribed sphere (V_{cir}).
Diameter sphericity [33]	$S_D = \frac{D_e}{D_c}$	The ratio of the diameter of a sphere having the same volume as the original particle $(D_{e,3})$ to the diameter of the minimum circumscribed sphere $(D_{e,3})$.
Sphere ratio sphericity [34]	$S_C = \frac{D_i}{D_c}$	The ratio of the diameter of the largest inscribing sphere of the particle $(D_{i,3})$ to the smallest circumscribed sphere of the particle $(D_{c,3})$.
Surface area sphericity [35]	$S_A = \frac{A_e}{A_s}$	The ratio of the surface area of the sphere having the same volume as the particle (A_e) to the real surface area of the particle (A_s) .
Roundness Roundness [33,36,37]		radius of curvatures of corners the maximum inscribed sphere

in Fig. 1(b) consists of 26,381 triangles and 12,866 vertices. The surface area of a given particle is the sum of areas of all the triangular faces. A small tetrahedron is formed by connecting three vertices and the particle's centroid (O) as shown in Fig. 1(c), and the volume of this tetrahedron is computed. The volume of the 3D particle (V) can then be determined by the sum of the volumes of all such tetrahedrons. For the 3D particle in Fig. 1(a), the computed surface area and volume are

 2.93×10^3 mm² and 1.06×10^4 mm³, respectively. For the 2.5D particle in Fig. 1(b), the same approach can be used to compute the surface area and volume, and thus, the results are 3.30×10^3 mm² and 1.22×10^4 mm³, respectively.

The maximum inscribing sphere is determined using a 3D Euclidean distance map as shown in Fig. 2(a). The maximum distance value in the 3D Euclidean distance map identifies the radius of the maximum

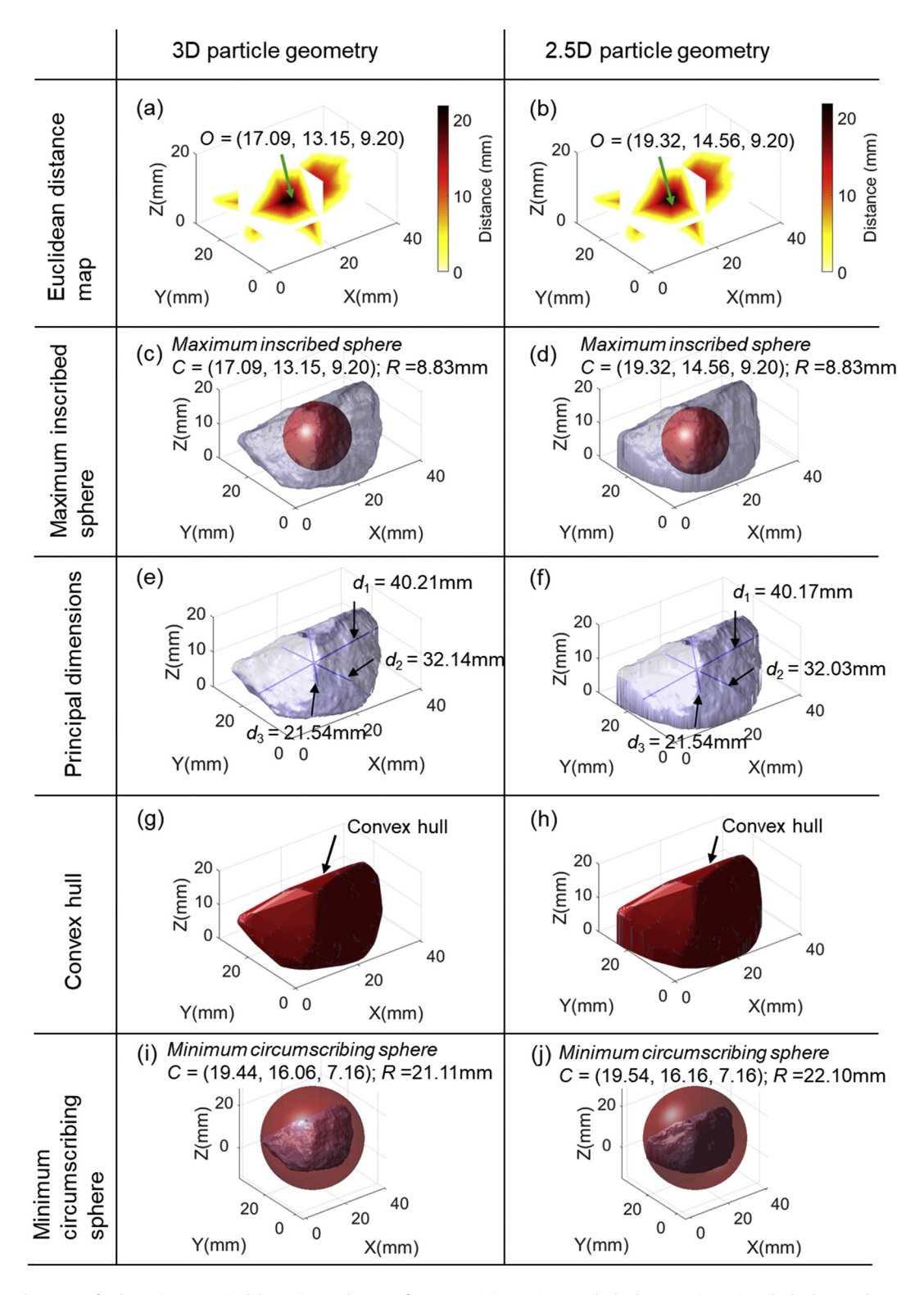


Fig. 2. Computational geometry for determining principal dimensions, volume, surface area, minimum circumscribed sphere, maximum inscribed sphere, and 3D convex hull of 3D and 2.5D particle geometries.

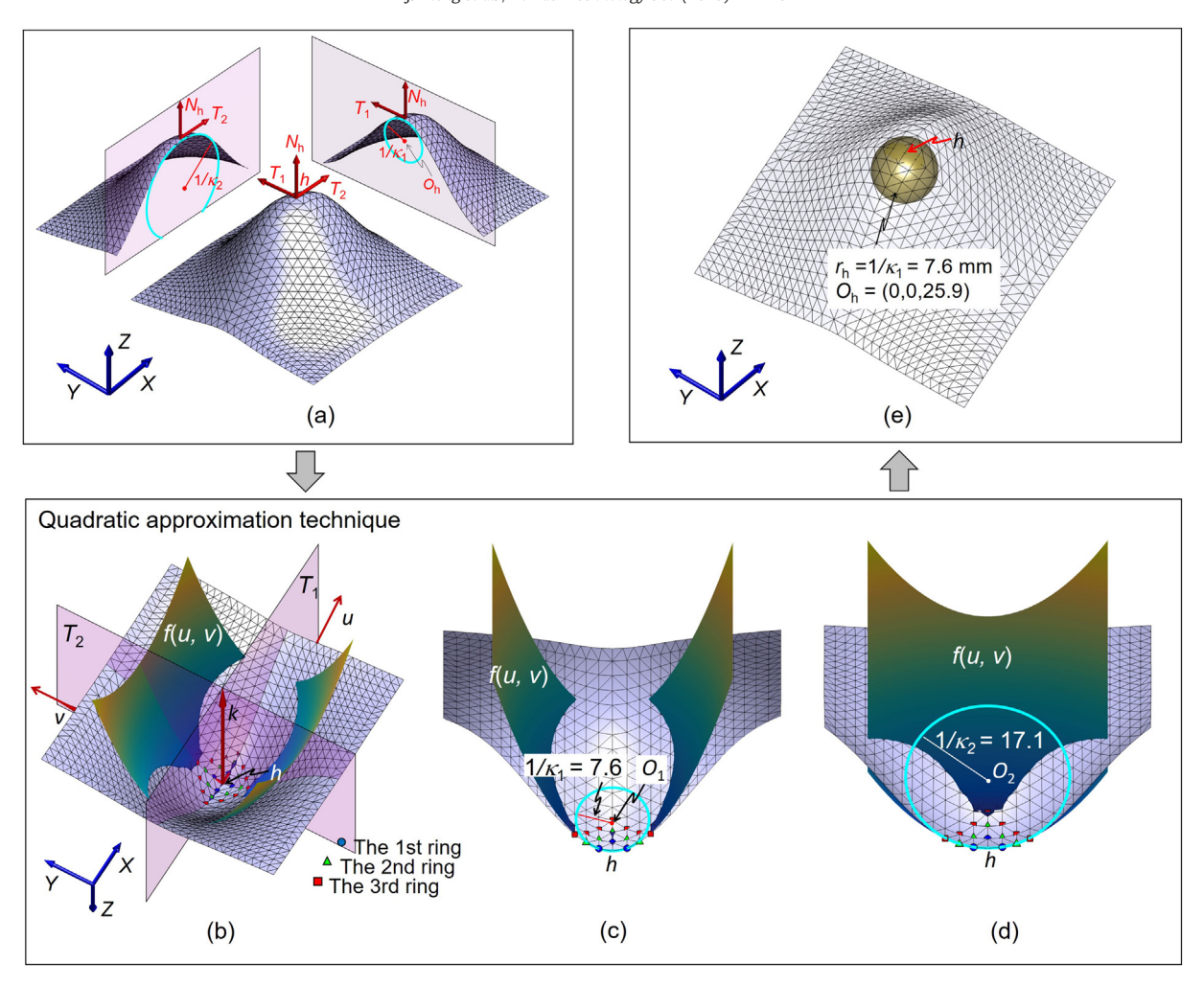


Fig. 3. The maximum and minimum normal curvatures of a 3D corner by the quadratic approximation technique.

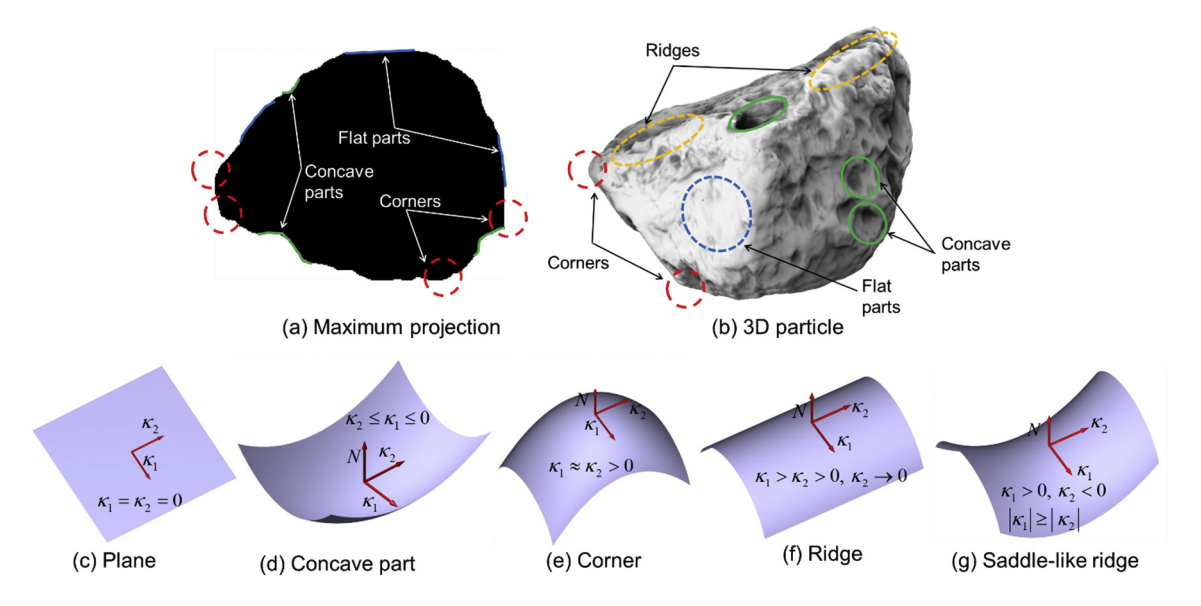


Fig. 4. The structural elements of 3D particle surfaces.

inscribed sphere of the particle. The coordinates of the maximum distance value identify the center of the maximum inscribed sphere of the particle. The computed maximum inscribed sphere is superimposed within the particle in Fig. 2(c). The same process is used to compute the maximum inscribed sphere for the 2.5D particle, and results are shown in Fig. 2(b) and (d).

The principal component analysis (PCA) is used to compute the length (d_1) , width (d_2) , and thickness (d_3) of a given particle geometry [27]. All the vertices of a 3D particle are considered as a point cloud in 3D

space. PCA can identify the largest variance of the point cloud, which is called the first principal component. The length of the first principal component is the length (d_1) of a 3D particle. Subsequently, PCA identifies the second largest variance, the second principal component, which is perpendicular to the first principal component and is the width (d_2) of the particle. The third principal component is perpendicular to both first and second principal components and identifies the thickness (d_3) of the particle. Fig. 2(e) and (f) illustrate the results of a PCA analysis, and the computed d_1 , d_2 , and d_3 values for the 3D and

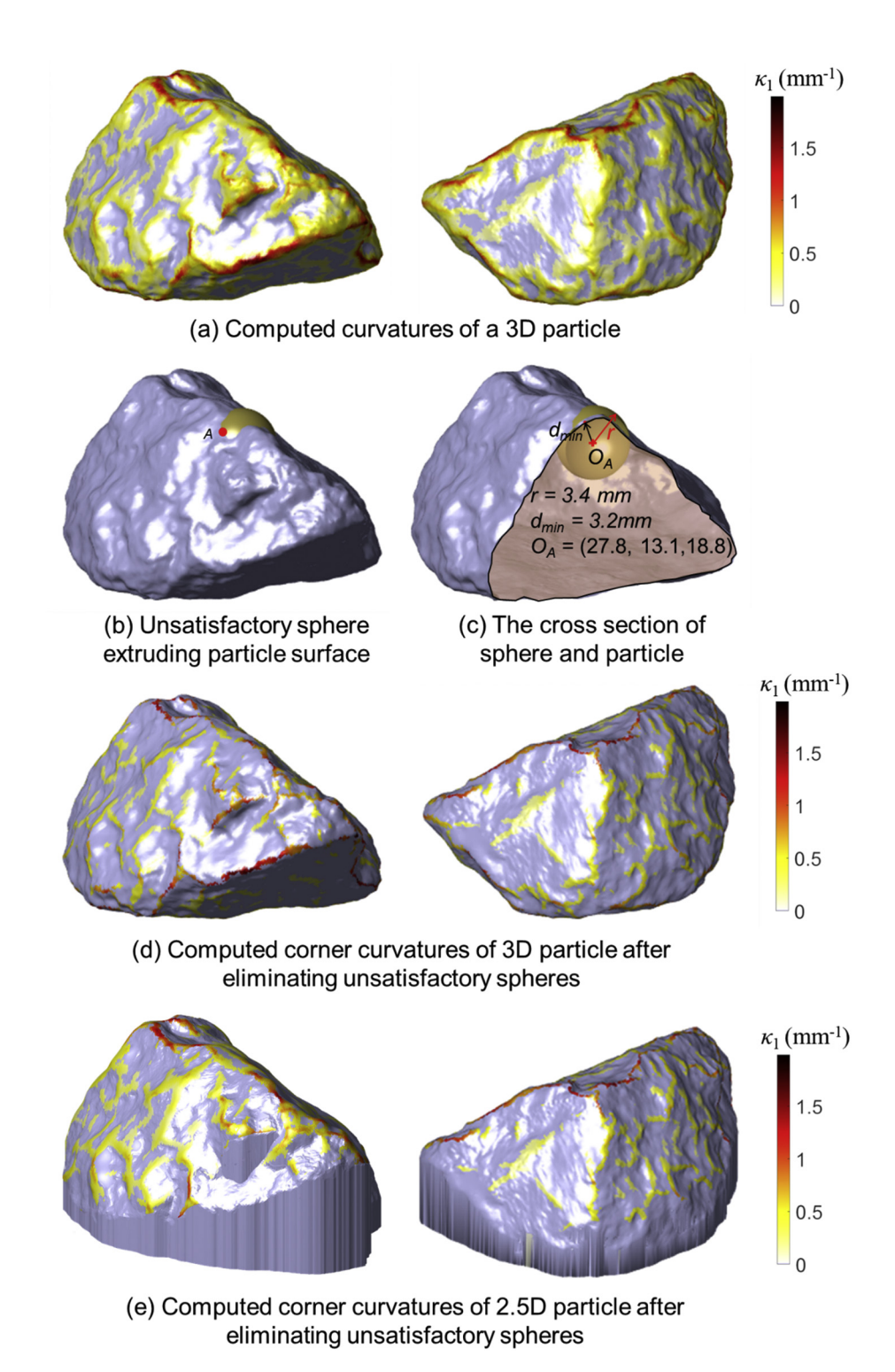


Fig. 5. Identification of corners and ridges on 3D and 2.5D particles.

2.5D particles, respectively. The 3D convex hull is determined by computing a minimum bounding surface circumscribing the particle as shown in Fig. 2(g) and (h). The minimum circumscribing sphere is determined by moving and expanding the previously determined maximum inscribed sphere until it tightly constraints particle surface as shown in Fig. 2(i) and (j).

After determining these parameters, the sphericity descriptors for 3D particle are computed as $C_{\rm x,3}=0.89$ (convexity), $C_{\rm 3}=0.71$ (circularity), $S_{\rm l,3}=0.75$ (intercept sphericity), $S_{\rm V,3}=0.31$ (volume sphericity), $S_{\rm D,3}=0.68$ (diameter sphericity), $S_{\rm C,3}=0.44$ (sphere ratio sphericity), and $S_{\rm A,3}=0.69$ (surface area sphericity). The sphericity descriptors for 2.5D particle are computed as $C_{\rm x,3}=0.87$, $C_{\rm 3}=0.75$, $S_{\rm l,3}=0.74$, $S_{\rm V,3}=0.33$, $S_{\rm D,3}=0.83$, $S_{\rm C,3}=0.45$, and $S_{\rm A,3}=0.79$. For this particle, the eight shape descriptors computed from 3D particle geometry and from 2.5D particle geometry are close to each other.

2.2. Computational geometry algorithm for determining roundness

As shown in Table 1, the computation of roundness requires determining curvatures of corners and the maximum inscribed sphere. The maximum inscribed sphere has been determined by the Euclidean distance algorithm, as shown in Fig. 2(a) to (d). This section focuses on determining the curvatures of corners.

For a vertex on a 3D corner as shown in Fig. 3(a), the curvature of this vertex is not a constant value but varies depending on the slicing directions. Therefore, the maximum and minimum normal curvatures κ_1 and κ_2 along with T_1 and T_2 directions are defined as principal curvatures as shown in Fig. 3(a). The T_1 and T_2 are called principal directions.

A quadratic approximation technique was used by this study to determine κ_1 and κ_2 values of corners. The 3D corner in Fig. 3(a) is used as an example to illustrate this technique. This 3D corner is transformed into the local coordinate system u-v-k in Fig. 3(b). The k axis is the opposite direction to the normal vector of h. The u and v axes are two tangent vectors of h and their directions are random. The neighbors of the vertex h can be classified by "rings" based on their connectivity to the vertex h as shown in Fig. 3(b). The points directly connecting to h are defined as the first ring. The points connecting to the first ring are defined as the second ring. Following the same trend, the third and fourth rings can be found.

As suggested by Gray et al. [28], this paper uses the vertex h and its neighbors on first, second, and third rings to fit a quadratic function f(u, v) using a least-square method:

$$f(u, v) = \frac{A}{2}u^2 + \frac{B}{2}v^2 + Cuv + Du + Ev$$
 (1)

For example, the coefficients of f(u, v) are determined as A = 0.0585, B = 0.1318, C = 0, D = 0, and E = 0 for this 3D corner. The fitted quadratic surface is superimposed to the original surface in Fig. 3(b). The Hessian matrix **H** of f(u, v) are computed as:

$$\mathbf{H} = \begin{bmatrix} \frac{\partial^2 f(u, v)}{\partial u \partial u} & \frac{\partial^2 f(u, v)}{\partial u \partial v} \\ \frac{\partial^2 f(u, v)}{\partial v \partial u} & \frac{\partial^2 f(u, v)}{\partial v \partial v} \end{bmatrix} = \begin{bmatrix} A & C \\ C & B \end{bmatrix}$$
 (2)

The principal curvatures κ_1 and κ_2 are the eigenvalues of **H** and the principal directions T_1 and T_2 are the eigenvectors of **H** [28]. In this example, the κ_1 and κ_2 are computed as 0.1318 and 0.0585 respectively, and the T_1 and T_2 are computed as (1,0,0) and (0,1,0), respectively. Fig. 3(c) and (d) show the cross-sections of T_1 and T_2 , respectively. The f(u,v) fits the surface at h and its neighbors in the first three rings. The $1/\kappa_1$ and $1/\kappa_2$ determines the radii of circles fitted to cross-sections in T_1 and T_2 directions.

The best-fitting sphere to the 3D corner is identified by the maximum normal curvatures κ_1 and its principal direction identified by T_1 slice. The radius of the best fitting sphere is $1/\kappa_1$ and the center of the best sphere O_h is $(0, 0, 1/\kappa_1)$ in the local u-v-k coordinate system. The sphere O_h is transferred back into the global X-Y-Z coordinate system as shown in Fig. 3(e), which fits the 3D corner very well. This is the process of finding the curvature for a vertex on a 3D corner of particle.

The 2D particle projection of a soil particle has a simple structure, which only includes three distinctive features: corners, flat particles, and concave parts as shown in Fig. 4(a). However, a 3D soil particle surface structure is complicated as shown in Fig. 4(b), which includes concave parts, flat parts, corners, and ridges. The majority of protrusions of a 3D particle surface are ridges. The corners of a 3D particle surface are essentially the intersections of several ridges. However, ridges are either occluded or projected as flat parts in 2D particle projections. In 3D particle assembly, the ridges and corners interlock with each other to create the load-bearing skeleton. Therefore, ridges can also be considered as "elongated corners" when evaluating the roundnesses of 3D particles.

The κ_1 and κ_2 can be used to discriminate the flat part, concave part, corners, ridges, and saddle-like ridges on the soil particle surface as well. Both κ_1 and κ_2 of a flat surface equal zero as shown in Fig. 4(c). For a concave part in Fig. 4(d), the computed κ_1 and κ_2 values are negative. For the corner part in Fig. 4(e), both κ_1 and κ_2 are positive, and they are close to each other. For the ridge in Fig. 4(f), the κ_1 in the bending direction is positive, while the κ_2 in the non-bending direction is close to zero. For the saddle ridge in Fig. 4(g), the surface bends in two directions oppositely. Therefore, κ_1 and κ_2 have opposite signs. Based on the κ_1 and κ_2 values, we can identify the corner and ridge parts on 3D soil particle surface by selecting vertices that satisfy $\kappa_1 > 0$.

The above technique was used to analyze the 3D particle in Fig. 5(a) to determine κ_1 and κ_2 values for each vertex. Out of 22,383 vertices, a total of 12,630 vertices had $\kappa_1 > 0$. These vertices are colored on particle surface based on their κ_1 values as shown in Fig. 5(a) in two different view directions.

Knowing κ_1 values of these 12,630 vertices, the radii and centers of the 12,630 best fitting spheres are determined following the pseudocode:

Step 1. Select a vertex e on the particle surface, and the κ_1 value of vertex e is $\kappa_{1.e}$.

Step 2. Determine the normal of this vertex e.

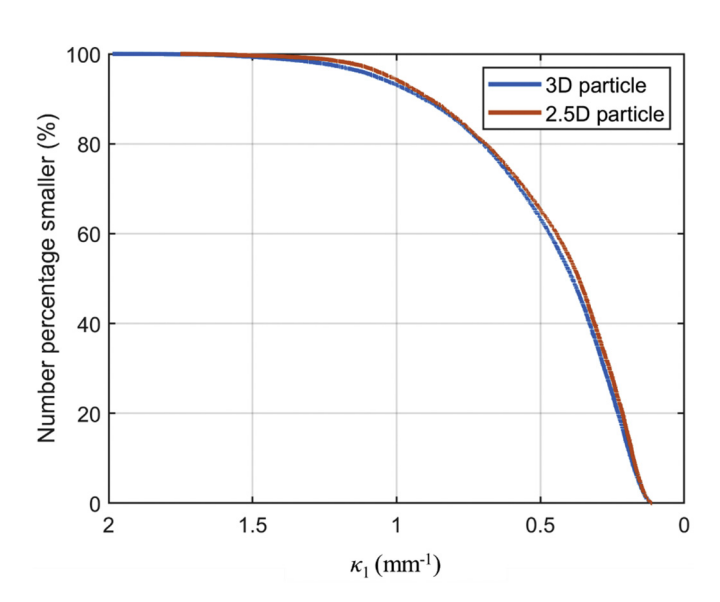


Fig. 6. The curvature distributions of vertices on 3D and 2.5D particles.

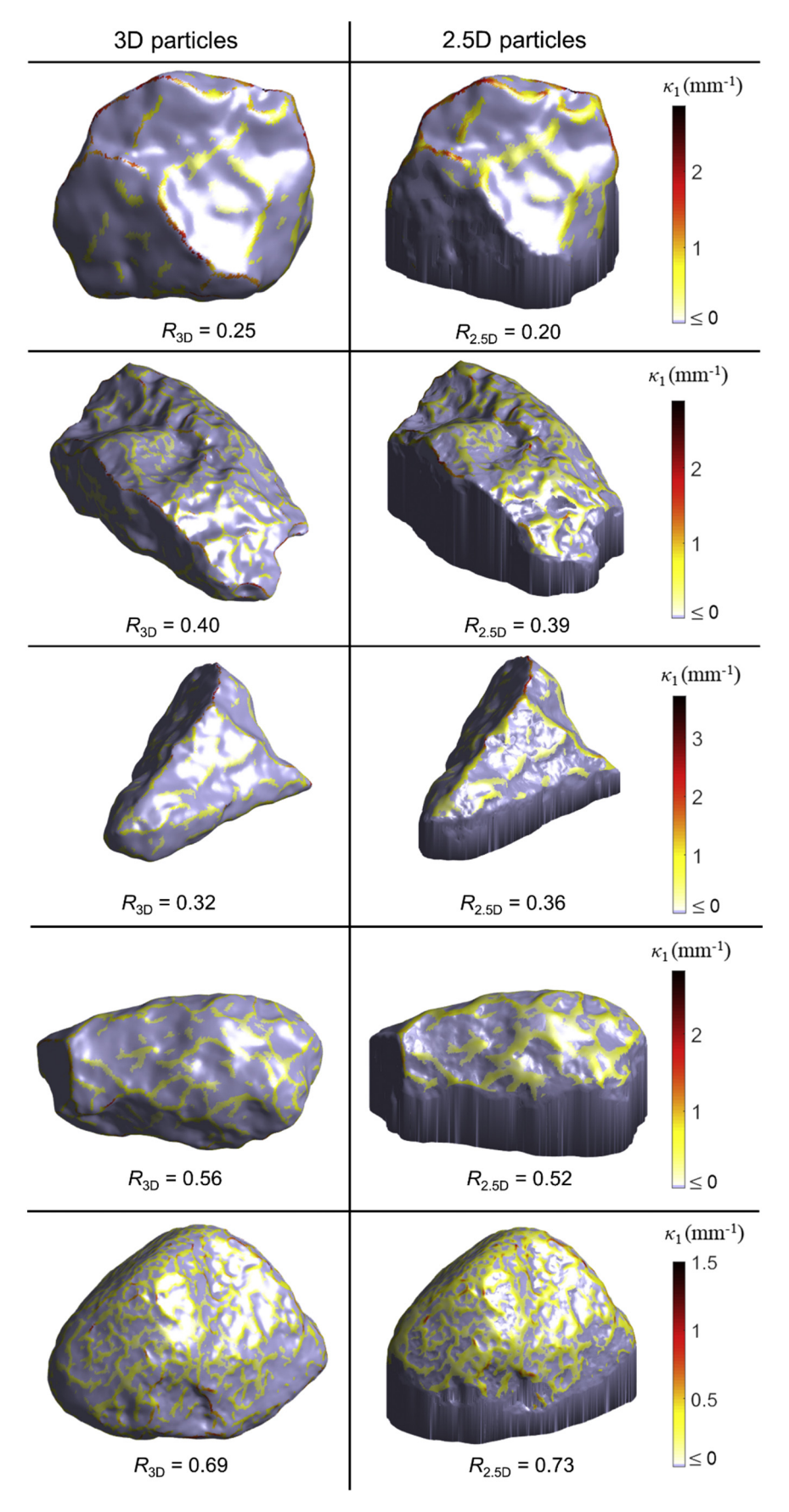


Fig. 7. The roundness computational results for some 3D and 2.5D particles.

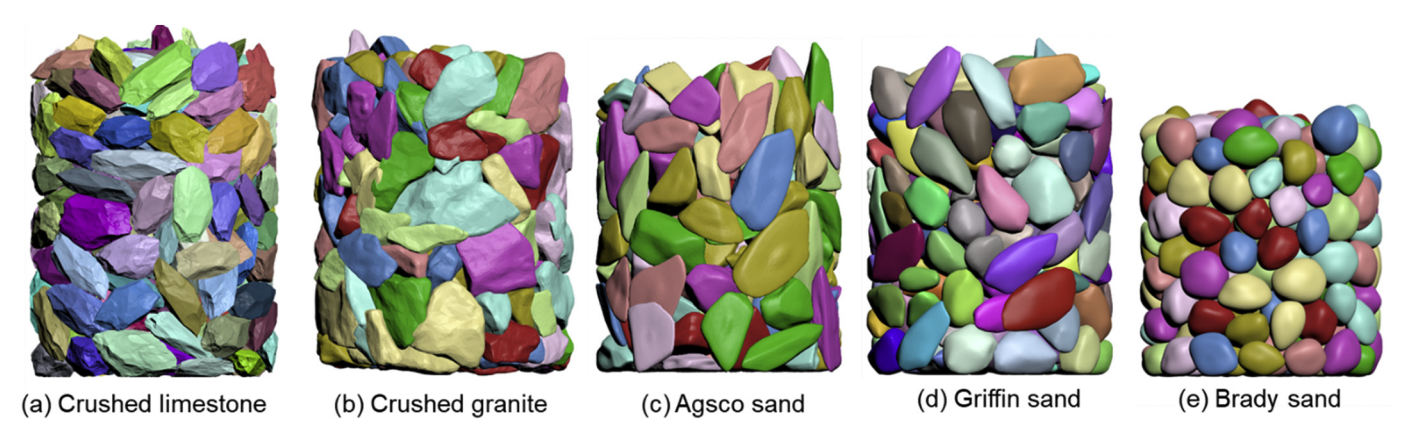


Fig. 8. Five coarse sand specimens scanned by X-ray CT.

Step 3. Along the normal, identify a point 0 and the distance between 0 and e is $1/\kappa_{1,e}$.

Step 4. The point 0 is the center of the best fitting sphere to e, and the radius of the best fitting sphere is $1/\kappa_{1,e}$.

The best-fitting spheres locally fit the vertices and their neighbors in the first three rings. Some spheres may not fit vertices of other parts of the 3D particle surface, and therefore, may extrude the particle surface. For example, in Fig. 5(b), the best fitting sphere at the vertex *A* extrudes particle surface. An algorithm is developed to address this issue.

The minimum distance between the center of each best fitting spheres and the particle surface is computed as d_{\min} . For example, for vertex A, the minimum distance between center O_A and particle surface is computed as $d_{\min} = 3.2$ mm in Fig. 5(c). Then, the d_{\min} is compared to sphere radius r_A . If $d_{\min} < r_A$ as shown in Fig. 5(c), the fitted sphere extrudes particle surface and the best sphere at the vertex A should be eliminated. If $d_{\min} = r$, the best fitting sphere of this vertex is satisfactory. In practice, it is rare that d_{\min} is exactly equal to r due to computational round-off. In fact, we found $d_{\min}/r > 0.99$ is accurate enough.

The vertices with their best fitting spheres satisfying $d_{min}/r > 0.99$ are kept for the next step. Other vertices are eliminated from 12,630

vertices. After this operation, a total of 6842 points are kept for the particle, which are plotted on the particle surface and colored based on their κ_1 values as shown in Fig. 5(d). These 6842 points identify the curvatures of corners and ridges on the 3D particle surface. Therefore, the average radius of curvatures of corners in the roundness definition in Table 1 can be further derived as:

Average radius of curvatures of corners
$$=\frac{1}{N}\sum_{i=1}^{N}\frac{1}{\kappa_{1,i}}$$
 (3)

Where the *N* is the number of vertices on corners and ridges, $1/\kappa_{1,i}$ is the radius of curvature at the *i*-th vertex on corners and ridges. The computed average radius of curvatures of corners for this 3D particle is 3.97 mm.

The roundness are computed as:

$$R = \frac{\frac{1}{N} \sum_{i=1}^{N} \frac{1}{\kappa_{1,i}}}{r_{in}} \tag{4}$$

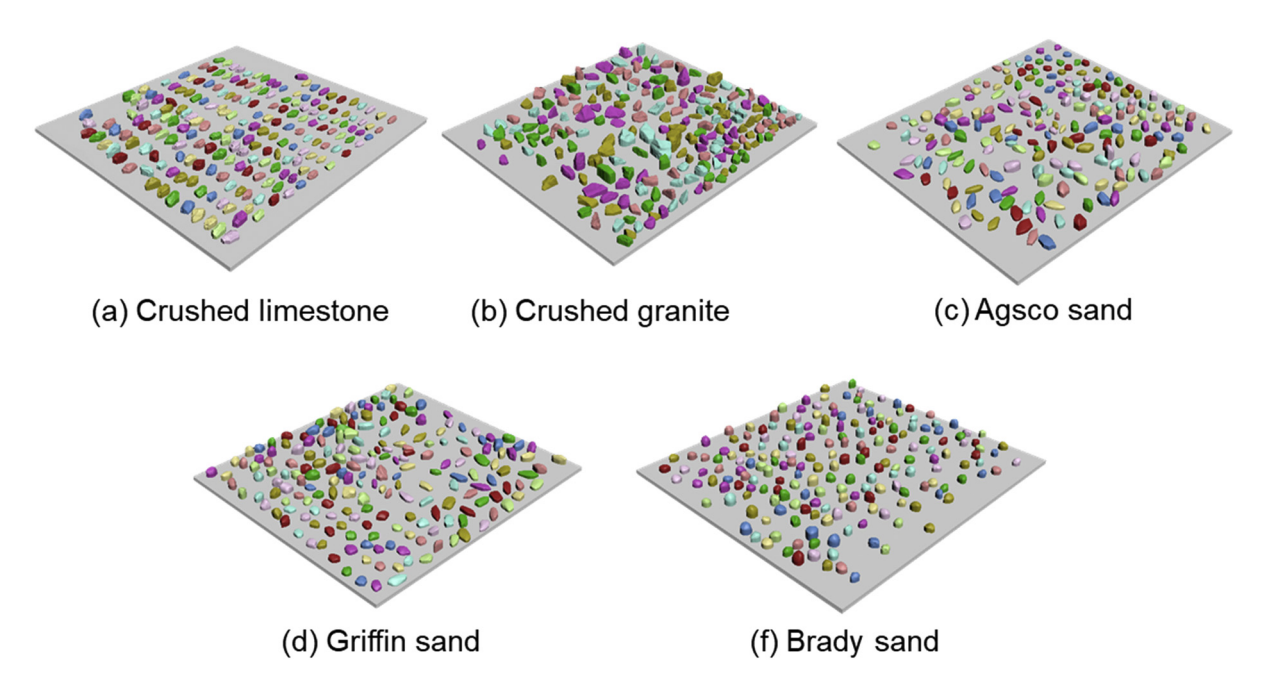


Fig. 9. The 2.5D particles by the structured light technique developed by Sun et al. [24].

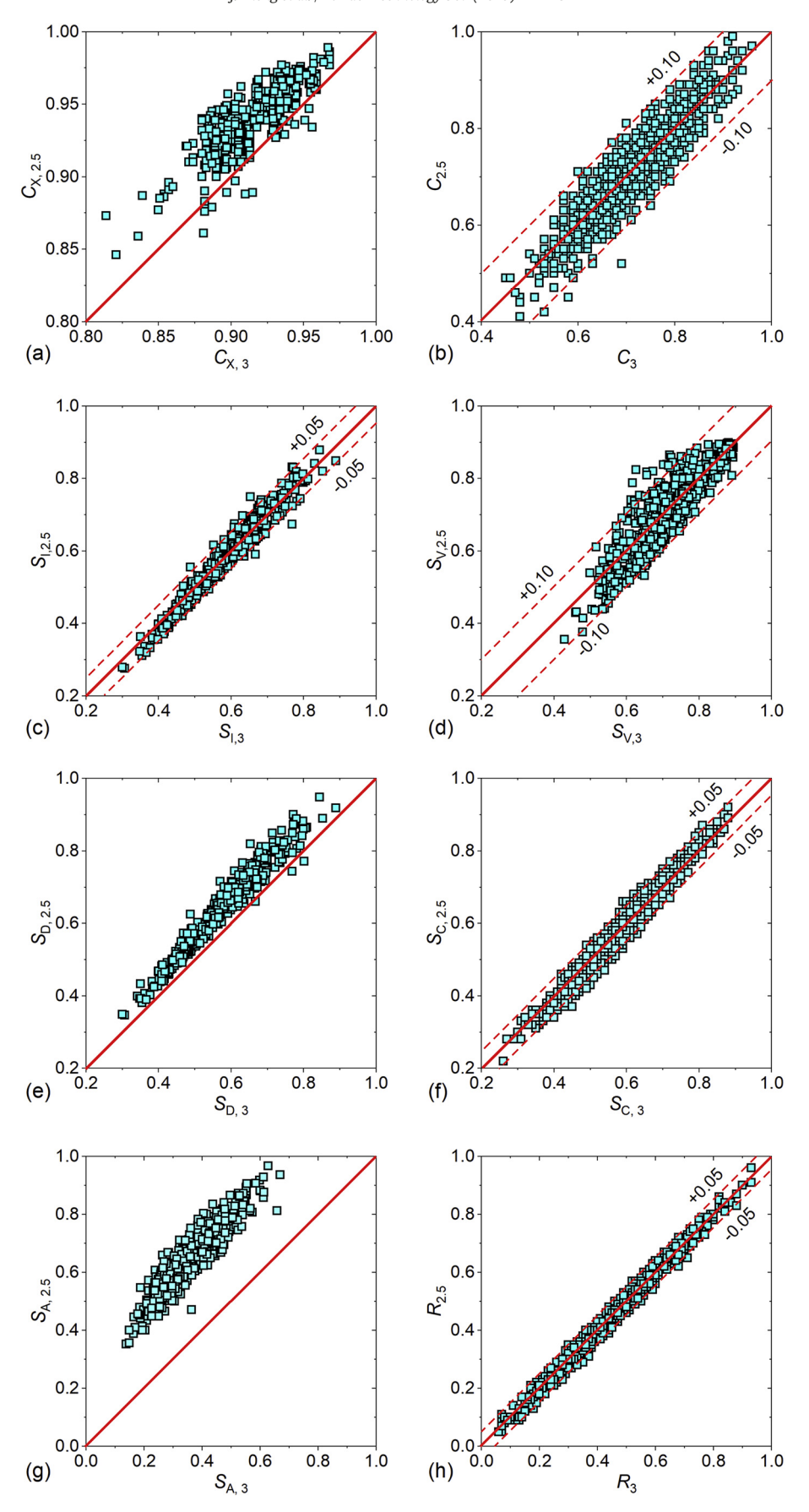


Fig. 10. The particle shape descriptors computed from 3D and 2.5D particle geometries.

Where $r_{\rm in}$ is the radius of the maximum inscribed sphere, which are computed using the Euclidean distance map. As shown in Fig. 2(a), the $r_{\rm in}$ is computed as 8.83 mm for this 3D particle. Therefore, the R is computed as 0.45.

For the 2.5D particles, the occluded parts are perpendicular to the table surface. Based on this property, we can identify occluded parts of 2.5D particles. Then, the occluded parts are excluded in analysis. The proposed computational geometry approach is used to identify corners and ridges on 2.5D particles and compute their curvatures. The results are shown in Fig. 5(e). The computed average radius of curvatures of corners for this 2.5D particle is 4.25 mm. As shown in Fig. 2(b), the $r_{\rm in}$ is computed as 8.82 mm. Therefore, the computed R is 0.48.

The computed κ_1 distributions of 3D and 2.5D particles are compared in Fig. 6. Although the 2.5D geometry only contains half particle geometry, the 2.5D geometry successfully captures the representative curvatures of the 3D geometry. Therefore, the computed R values are very close between 2.5D and 3D geometries.

The above computational geometry algorithm is used to analyze five other 3D particles and their 2.5D particles in Fig. 7. The developed algorithm successfully analyzes particles from angular to well-rounded. The computed *R* values are also superimposed in the image. The *R* values computed from 3D and 2.5D particles agree well with each other, with a divergence of within 0.05.

3. Results

Five sand specimens were used in this study, including crushed limestone (very angular particles), crushed granite (very angular to angular particles), Agsco sand (angular to sub-angular particles), Agsco sand (subangular to sub-rounded particles), Griffin sand (sub-rounded to well-rounded particles), and Ottawa sand (rounded to well-rounded particles). For each sand, we manually picked 200 particles in size range of #6 sieve (3.35 mm) to #8 sieve (2.36 mm). These particles were funneled into a plastic cylinder to generate specimens.

A high-resolution X-ray CT was used to scan the soil specimen with a spatial resolution of 12 μ m/voxel. Having obtained 3D volumetric images, individual soil particles were identified by image segmentation techniques. The first step was to use image thresholding techniques [29] to segment air and particles. This resulted in a binary image, in which the soil particles had a voxel value of ones (white color), and the air had a voxel value of zeros (black color). In this binary image, the soil particles were contacting with each other. Therefore, the second step was to use an improved watershed analysis technique proposed by Sun et al. [27] to segment contacting particles. The results are shown in Fig. 8. After segmentation, 200 particles were identified for each sand, which was the same as the number of used particles during specimen preparation.

After X-ray CT scan, each specimen was spread on a flat plane and captured by the structured light system developed by Sun et al. [24]. The contacting particles can also be segmented by the improved watershed analysis [27]. The results are shown in Fig. 9.

The eight particle shape descriptors in Table 1 are computed for all the 3D and 2.5 particles using the computational geometry technique developed by this study. The results are shown in Fig. 10. The $C_{\rm x}$ (convexity), $S_{\rm D}$ (diameter sphericity), and $S_{\rm A}$ (surface area sphericity) computed from 2.5D particles overestimate these values computed from 3D particles as shown in Fig. 10(a), (e), and (g). The C (circularity) and $S_{\rm V}$ (volume sphericity) computed from 2.5D particles agree well with these values computed from 3D particles with a divergence of within ± 0.10 as shown in Fig. 10(b) and (d). The $S_{\rm I}$ (intercept sphericity), $S_{\rm C}$ (sphere ratio sphericity), and R (roundness) agree excellently with these values computed from 3D particles with a divergence of within ± 0.05 as shown in Fig. 10(c), (f), and (h).

The following correction factors are developed to correct the convexity, diameter sphericity, and surface area sphericity computed from 2.5D particles to better estimate these values computed from 3D particles:

Corrected
$$C_{x,2.5} = C_{x,2.5} - 0.30$$
 (5)

Corrected
$$S_{D.2.5} = S_{D.2.5} - 0.60$$
 (6)

Corrected
$$S_{A,2.5} = S_{A,2.5} - 0.28$$
 (7)

The corrected convexity, diameter sphericity, and surface area sphericity are plotted against these values computed from 3D particles in Fig. 11. Good agreements are observed. The divergence of 2.5D and 3D convexity is within ± 0.025 . The divergence of 2.5D and 3D diameter sphericity is within ± 0.05 . The divergence of 2.5D and 3D surface area sphericity is within ± 0.010 .

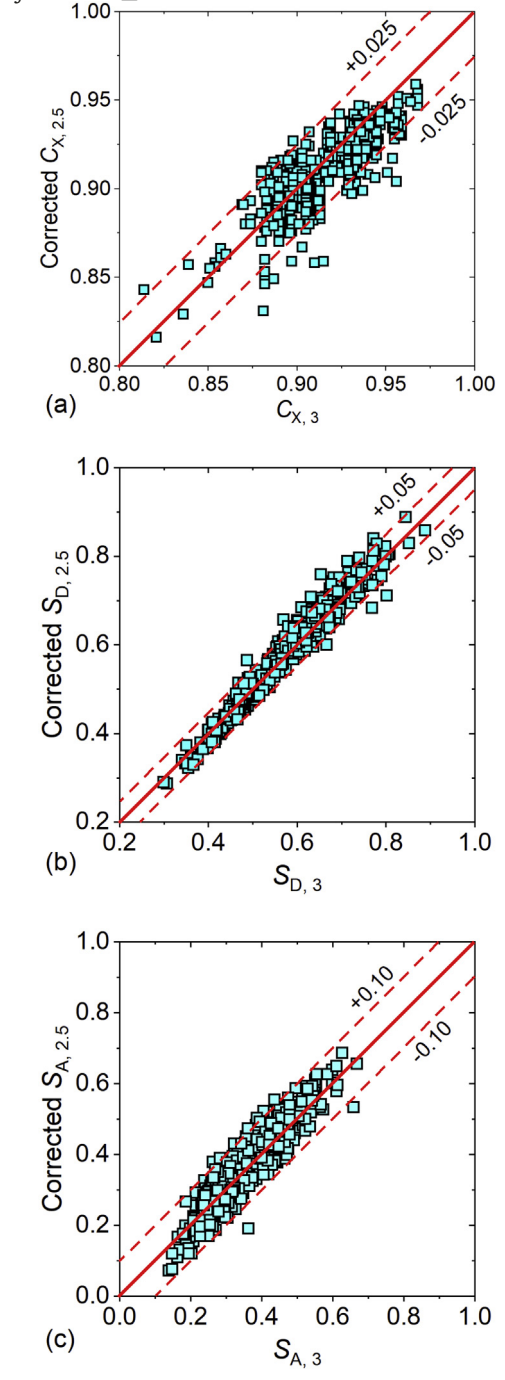


Fig. 11. The corrected the convexity, diameter sphericity, and surface area sphericity.

4. Conclusion

Many 3D imaging techniques used by geotechnical engineers can only capture half particle geometries, such as stereophotography, laser scanner, and structured light. These imaging systems can capture upper-half particle surface geometry visible to the camera view but cannot capture the lower-half particle surface geometry occluded from the camera view.

This paper evaluated the accuracy of using upper-half particle geometries, which was defined as 2.5D images, to characterize particle shapes of the complete 3D particle geometries. Eight commonly used particle shape descriptors were considered in this research, including convexity, circularity, intercept sphericity, volume sphericity, diameter sphericity, sphere ratio sphericity, surface area sphericity, and roundness. A series of 3D computational geometry techniques were developed to compute these shape descriptors.

Five coarse sand specimens were scanned by X-ray CT and structured lighted to generate 3D and 2.5D particle geometries. The 3D computational geometry technique was used to compute eight shape descriptors for these particles. The results of 3D and 2.5D geometries were compared. The convexity, diameter sphericity, and surface area sphericity computed from 2.5D particles overestimated these values computed from 3D particles. The circularity and volume sphericity computed from 2.5D particles agreed well with these values computed from 3D particles with a divergence of within ± 0.10 . The intercept sphericity, sphere ratio sphericity, and roundness agreed excellently with these values computed from 3D particles with a divergence of within ± 0.05 .

Three equations were developed to correct the convexity, diameter sphericity, and surface area sphericity computed from 2.5D particles. After correction, these values well matched the values computed from 3D particles. The divergence of 2.5D and 3D convexity is within \pm 0.025. The divergence of 2.5D and 3D diameter sphericity is within \pm 0.05. The divergence of 2.5D and 3D surface area sphericity is within \pm 0.010.

Declaration of Competing Interest

The authors declare that they have no conflict of interest.

Acknowledgments

This material is based upon work supported by the U.S. National Science Foundation under Grant No. CMMI 1917332. Any opinions, findings, and conclusions or recommendations expressed in this material are those of the authors and do not necessarily reflect the views of the National Science Foundation.

References

- [1] F.N. Altuhafi, M.R. Coop, V.N. Georgiannou, Effect of particle shape on the mechanical properties of natural sands, J. Geotech. Geoenviron. Eng. 142 (2016) 1–15, https://doi.org/10.1061/(ASCE)GT.1943-5606.0001569.
- [2] R. Kandasami, T. Murthy, Effect of particle shape on the mechanical response of a granular ensemble, Geomech. Micro Macro (2014) 1093–1098, https://doi.org/10. 1201/b17395-196.
- [3] Y. Xiao, L. Long, T. Matthew Evans, H. Zhou, H. Liu, A.W. Stuedlein, Effect of particle shape on stress-dilatancy responses of medium-dense sands, J. Geotech. Geoenviron. Eng. 145 (2018), 04018105. https://doi.org/10.1061/(asce)gt.1943-5606.0001994.
- [4] P. Vangla, N. Roy, M.L. Gali, Image based shape characterization of granular materials and its effect on kinematics of particle motion, Granul. Matter 20 (2017) https://doi. org/10.1007/s10035-017-0776-8.
- [5] J. Zheng, R.D. Hryciw, Index void ratios of sands from their intrinsic properties, J. Geotech. Geoenviron. Eng. 142 (2016) 1–10, (06016019) https://doi.org/10.1061/(ASCE)GT.1943-5606.0001575.
- [6] W.C. Krumbein, Measurement and geological significance of shape and roundness of sedimentary particles, SEPM J. Sediment. Res. 11 (1941) https://doi.org/10.1306/ d42690f3-2b26-11d7-8648000102c1865d.
- [7] W.C. Krumbein, L.L. Sloss, Stratigraphy and Sedimentation, W.H. Freeman and Company, San Francisco, 1951.

- [8] M.C. Powers, A new roundness scale for sedimentary particles, SEPM J. Sediment. Res. 23 (1953) https://doi.org/10.1306/d4269567-2b26-11d7-8648000102c1865d.
- [9] R.D. Hryciw, J. Zheng, K. Shetler, Comparison of particle roundness and sphericity by traditional chart and computer methods, J. Geotech. Geoenviron. Eng. 142 (2016), 04016038. https://doi.org/10.1061/(ASCE)GT.1943-5606.0001485.
- [10] J. Zheng, R.D. Hryciw, Traditional soil particle sphericity, roundness and surface roughness by computational geometry, Géotechnique 65 (2015) https://doi.org/ 10.1680/geot.14.P.192.
- [11] J. Zheng, R.D. Hryciw, Segmentation of contacting soil particles in images by modified watershed analysis, Comput. Geotech. 73 (2016) 142–152, https://doi.org/10.1016/j.compgeo.2015.11.025.
- [12] J. Zheng, R.D. Hryciw, Identification and characterization of particle shapes from images of sand assemblies using pattern recognition, J. Comput. Civ. Eng. 32 (2018) https://doi.org/10.1061/(ASCE)CP.1943-5487.0000765.
- [13] A.M. Druckrey, K.A. Alshibli, R.I. Al-Raoush, 3D characterization of sand particle-toparticle contact and morphology, Comput. Geotech. 74 (2016) 26–35, https://doi. org/10.1016/j.compgeo.2015.12.014.
- [14] K.-W.W. Lim, R. Kawamoto, E. Andò, G. Viggiani, J.E. Andrade, Multiscale characterization and modeling of granular materials through a computational mechanics avatar: a case study with experiment, Acta Geotech. 11 (2015) 243–253, https://doi. org/10.1007/s11440-015-0405-9.
- [15] K.A. Alshibli, M.F. Jarrar, A.M. Druckrey, R.I. Al-Raoush, R.I. Al-Raoush, Influence of particle morphology on 3D kinematic behavior and strain localization of sheared sand, J. Geotech. Geoenviron. Eng. 143 (2017) 4016097, https://doi.org/10.1061/ (asce)gt.1943-5606.0001601.
- [16] B. Zhou, J. Wang, Random generation of natural sand assembly using micro x-ray to-mography and spherical harmonics, Géotechn. Lett. 5 (2015) 6–11, https://doi.org/10.1680/geolett.14.00082.
- [17] B. Zhou, J. Wang, Generation of a realistic 3D sand assembly using X-ray micro-computed tomography and spherical harmonic-based principal component analysis, Int. J. Numer. Anal. Methods Geomech. 41 (2016) 93–109, https://doi.org/10.1002/nag.2548.
- [18] D. Kong, J. Fonseca, Quantification of the morphology of shelly carbonate sands using 3D images, Géotechnique 68 (2018) 249–261, https://doi.org/10.1680/jgeot.
- [19] Z. Lai, Q. Chen, Reconstructing granular particles from X-ray computed tomography using the TWS machine learning tool and the level set method, Acta Geotech. 14 (2019) 1–18, https://doi.org/10.1007/s11440-018-0759-x.
- [20] E. Andò, G. Viggiani, S.A. Hall, J. Desrues, Experimental micro-mechanics of granular media studied by x-ray tomography: recent results and challenges, Geotech. Lett. 3 (2013) 142–146, https://doi.org/10.1680/geolett.13.00036.
- [21] H. Kim, C.T. Haas, A.F. Rauch, C. Browne, Dimensional ratios for stone aggregates from three-dimensional laser scans, J. Comput. Civ. Eng. 16 (2002) 175–183, https://doi.org/10.1061/(ASCE)0887-3801(2002)16:3(175).
- [22] J. Zheng, R.D. Hryciw, Soil particle size characterization by stereophotography, Geotech. Spec. Publ. (2014) 64–73, https://doi.org/10.1061/9780784413272.007.
- [23] J. Zheng, R.D. Hryciw, Soil particle size and shape distributions by stereophotography and image analysis, Geotech. Test. J. 40 (2017) 317–328, https://doi.org/10. 1520/GTJ20160165.
- [24] Q. Sun, Y. Zheng, B. Li, J. Zheng, Z. Wang, Three-dimensional particle size and shape characterisation using structural light, Géotech. Lett. 9 (2019) 72–78.
- [25] Y.S. Lee, T.C. Chang, Application of computational geometry in optimizing 2.5D and 3D NC surface machining, Comput. Ind. 26 (1995) 41–59, https://doi.org/10.1016/ 0166-3615(95)80005-0.
- [26] H.-S. Ohm, R.D. Hryciw, Translucent segregation table test for sand and gravel particle size distribution, Geotech. Test. J. 36 (2013) 20120221, https://doi.org/10.1520/gtj20120221.
- [27] Q. Sun, J. Zheng, C. Li, Improved watershed analysis for segmenting contacting particles of coarse granular soils in volumetric images, Powder Technol. 356 (2019) 295–303, https://doi.org/10.1016/j.powtec.2019.08.028.
- [28] A. Gray, E. Abbena, S. Salamon, Modern Differential Geometry of Curves and Surfaces with Mathematica, Third edition, Chapman & Hall/CRC, 2006.
- [29] N. Otsu, A threshold selection method from gray-level histograms, IEEE Trans. Syst. Man. Cybern. 9 (1979) 62–66.
- [30] C.F. Mora, A.K.H. Kwan, Sphericity, shape factor, and convexity measurement of coarse aggregate for concrete using digital image processing, Cem. Concr. Res. 30 (2000) 351–358, https://doi.org/10.1016/S0008-8846(99)00259-8.
- [31] B.C. Aschenbrenner, A new method of expressing particle sphericity, J. Sediment. Res. 26 (1956) 15–31, https://doi.org/10.1306/74D704A7-2B21-11D7-8648000102C1865D.
- [32] N.A. Riley, Projection sphericity, SEPM J. Sediment. Res. 11 (1941) https://doi.org/10. 1306/d426910c-2b26-11d7-8648000102c1865d.
- [33] H. Wadell, Sphericity and roundness of rock particles, J. Geol. 41 (1933) 310–331, https://doi.org/10.1086/624040.
- 34] J.C. Santamarina, G.C. Cho, Soil behaviour: the role of particle shape, Adv. Geotech. Eng. Skempt. Conf., Thomas Telford, London, London 2004, pp. 604–617.
- 35] C.-Y. Kuo, R. Freeman, Imaging indices for quantification of shape, angularity, and surface texture of aggregates, Transp. Res. Rec. J. Transp. Res. Board. 1721 (2000) 57–65, https://doi.org/10.3141/1721-07.
- [36] H. Wadell, Volume, shape, and roundness of rock particles, J. Geol. 40 (1932) 443–451, https://doi.org/10.1086/623964.
- [37] H. Wadell, Volume, shape, and roundness of quartz particles, J. Geol. 43 (1935) 250–280, https://doi.org/10.1086/624298.